# Stochastic modelling of aerosol deposition for LES of 90° bend turbulent flow

Abdallah S. Berrouk [a,*], Dominique Laurence [a,b,1]

[a] *The University of Manchester, MACE School, P.O. Box 88, Manchester M60 1QD, United Kingdom*
[b] *Electricite de France, R&D, MFEE, 6 Quai Watier 78400, Paris, France*

## Abstract

Aerosols deposition in turbulent bend flows is a major concern that is critical to many industrial, environmental and biomedical applications. In this work, a well-resolved LES was performed to compute the deposition efficiency of aerosols in turbulent circular cross-section bend flow of Dean number $De = 4,225$. The numerical predictions were compared to the experimental work of Pui et al. [Pui, D.Y.H., Romay-Novas, F., Liu, B.Y.H., 1987. Experimental study of particle deposition in bend of circular cross-section. Aerosol Sci. Technol. 7, 301–315] and the fully-resolved LES of Breuer et al. [Breuer, M., Baytekin, H.T., Matida, E.A., 2006. Prediction of aerosol deposition in 90° bends using LES and an efficient Lagrangian tracking method. J. Aerosol Sci. 37, 1407–1428]. In the present LES, a slightly coarser but unstructured-grid numerical description was adopted, entailing that a portion of the small scales' contribution to particle dispersion to be discarded. Thus, a Langevin-type stochastic model was used to model the effect of the discarded sub-grid motion on aerosol deposition. This stochastic model was shown to perform well in previous studies [Berrouk, A.S., Laurence, D., Riley, J.J., Stock, D.E., 2007. Stochastic modelling of inertial particle dispersion by subgrid motion for LES of high Reynolds number pipe flow. J. Turbulence, 8, 50]. Good care was taken to ensure that the main dynamical features of the continuous phase were captured by the present LES. An estimation of the filtered-out kinetic energy was provided. Results of the present LES with SGS model for particles were found to compare well with the experimental work and the fully-resolved LES (near-wall DNS) of Breuer for all the range of the Stokes number considered, $0.001 < St < 1.5$. Influence of the SGS model for particles was visible for the deposition efficiency of aerosols with Stokes number $St < 0.3$.
© 2008 Elsevier Inc. All rights reserved.

*Keywords:* LES; Aerosols deposition; Bend; Sub-grid; Stochastic

## 1. Introduction

Deposition of aerosols in turbulent bend flows is encountered in many industrial, environmental and biomedical applications of practical interest. Experimental and numerical studies of inertial deposition in curved pipes have been motivated by interest in calculating the deposition of inhaled particles in human airways. The aim is to help providing more effective treatment of lung diseases, better protection against toxic airborne pollutants, and improvement in routes of systemic drug administration (Finlay, 2001). Other applications consist of systems for sampling aerosol particles from atmosphere or industrial process streams that commonly occur in bends of piping systems. A significant loss of particles can take place in a bend as a result of inertial deposition. To obtain accurate data, it is important to correct for the losses of particles in bends as well as other parts of

---

* Corresponding author. Present address: Department of Building and Construction, City University of Hong Kong, Tat Chee Avenue, Kowloon City, Kowloon, Hong Kong. Tel.: +852 27844274.
  *E-mail addresses:* aberrouk@cityu.edu.hk, berrouks@yahoo.fr (A.S. Berrouk), dominique.laurence@edf.fr, dominique.laurence@manchester.ac.uk (D. Laurence).
[1] Tel.: +33 130 877257/+44 1613063704; fax: +44 1613063723.

## Nomenclature

*Roman letters*

| | |
|---|---|
| $\bar{p}$ | Filtered pressure field |
| $\overline{S}_{ij}$ | Resolved rate of strain tensor |
| $\bar{u}_i$ | Filtered fluid velocity |
| $\tilde{k}_{SGS}$ | Modified SGS kinetic energy |
| $k_{SGS}$ | SGS kinetic energy |
| $A_{s,i}$ | Drift vector |
| $B_{s,ij}$ | Diffusion matrix |
| $C_0^*$ | Diffusion coefficient |
| $C_0$ | Kolmogorov constant |
| $C_D$ | Drag coefficient |
| $C_n$ | Cunningham slip correction factor |
| $C_s$ | Smagorinsky constant |
| $d_p$ | Particle diameter |
| $De$ | Dean number $De = Re/\sqrt{R_0}$ |
| $k_{SGS}$ | SGS kinetic energy |
| $N_p^{after\ bend}$ | Number of particles that exit the bend |
| $N_p^{bend}$ | Number of particles that deposit in the bend |
| $R_0$ | Curvature ratio $R_0 = R_b/R$ |
| $R_b$ | Radius of curvature of the bend |
| $Re_\tau$ | Friction Reynolds number |
| $Re_p$ | Particle Reynolds number |
| $T_{SGS}^*$ | Fluid sub-grid time scale with inertia and CT effects included |
| $T_{E,SGS}$ | Eulerian sub-grid time scale |
| $T_E$ | Eulerian time scale |
| $T_{L,SGS}$ | Lagrangian sub-grid time scale |
| $T_L$ | Lagrangian time scale |
| $U_0$ | Mean velocity |
| $u_\tau$ | Friction or shear velocity |
| $u_p$ | Particle velocity |
| $u_r$ | Mean slip velocity between fluid and inertial particles |
| $u_s$ | Velocity of the fluid seen |
| $u_i$ | Fluid fluctuating turbulent velocity |
| $W_i$ | Wiener process |
| $x_i$ | Cartesian coordinate system directions |
| $x_p$ | Particle position |

| | |
|---|---|
| $y^+$ | Dimensionless distance from the wall |
| $g$ | Gravity force |
| $h$ | Grid spacing |
| $I$ | Inner radius of the curved bend |
| $k$ | Total Kinetic energy |
| $O$ | Outer radius of the curved bend |
| $R$ | Tube radius |
| $Re$ | Flow Reynolds number: $Re = u_b D/v$ |
| $St$ | Stokes number $St = \tau_p/T$ |
| $T$ | Integral time scale $T = R/U_0$ |
| $t$ | Time |

*Greek letters*

| | |
|---|---|
| $\beta$ | Ratio between the Lagrangian and the Eulerian time scales |
| $\Delta t$ | Time step |
| $\Delta$ | Filter width |
| $\delta_{ij}$ | Kornecker Delta |
| $\epsilon_r$ | Dissipation rate of the SGS kinetic energy |
| $\eta_p$ | Deposition efficiency |
| $v$ | Kinematic fluid viscosity |
| $v_{SGS}$ | Sub-grid scale eddy viscosit. |
| $\rho_f$ | Fluid density |
| $\rho_p$ | Particle density |
| $\tau_{ij}$ | Sub-grid stress tensor |
| $\tau_p$ | Particle response time |
| $\tau_w$ | Wall shear stress $\tau_w = \rho_f u_\tau^2$ |

*Acronyms*

| | |
|---|---|
| CT | Cross Trajectory |
| DNS | Direct Numerical Simulation |
| LES | Large Eddy Simulation |
| RANS | Reynolds-Averaged Navier-Stokes |
| SDE | Stochastic Differential Equation |
| SGS | Sub-Grid Scale |
| SM | Stochastic Model |

the sampling system. This is a major concern for High-Tech industries such as semiconductor manufacturing. For the oil and gas industry, predicting inertial particle deposition and the accompanying erosion phenomena is crucial to avoiding extremely expensive component repair, replacement or failure, and by consequence expensive system shutdown.

For many of these applications, a Direct Numerical Simulation (DNS) is not practical with today's computers while the Reynolds-Averaged Navier-Stokes approach (RANS) is facing many limitations (Lakehal, 2002). Thus, Large Eddy Simulation (LES) has emerged as a promising tool to address these types of problems and its use has increased over the years.

Large eddy simulation is essentially an under-resolved simulation of the complex turbulence phenomenon that uses a model to account for the lack of small scale resolution. In LES, the conflicting requirements of complexity reduction while maintaining accurate predictions are achieved by coarsening the numerical description through spatial filtering on one hand and using a sub-grid stress (SGS) modelling on the other hand. In the filtering process the instantaneous information concerning the dynamics of the small scales is washed out.

In LES of dispersed turbulent multiphase flows, it has been common that tracking inertial particles in turbulent flows is carried out using only the filtered velocity field, considering as negligible any transport by the sub-grid

fluctuations. In principle, this should be sufficient to predict turbulent fluctuations and their effects on the transport of inertial particles with large relaxation times compared to the smallest LES-resolved turbulence time scales. However, in wall-bounded turbulent flows, the filtered-out small scales near the wall often carry a substantial amount of kinetic energy and the spatial resolution is not fine enough to capture them. This may result in an excessive filtering-out of kinetic energy. This is also the case for flows with recirculation zones and secondary motion. Thus, modelling turbulent fluctuations linked to these small scales has proven crucial for small-Stokes-number inertial particle dispersion as it was shown by Armenio et al. (1999) and Berrouk et al. (2007). This modelling is expected to be equally important for particle deposition.

The time dependent velocity field seen by the inertial particles in a Lagrangian framework can be stochastically constructed through the use of a stochastic diffusion process such as Langevin equation (Langevin, 1908). This Lagrangian approach based on Langevin equation has been extensively used in the framework of RANS to construct total turbulence fluctuations based on the mean flow statistics (Minier et al., 2004).

In the framework of RANS, the Lagrangian stochastic model is designed with the aim to reproduce the whole spectrum of turbulence that an inertial particle should see. This turbulence is, in particular in the case of non-equilibrium flows, highly anisotropic and characterized by a wide range of length and time scales. Modelling accurately such intricate details a turbulent flow-field is often problematic. This could explain the limitations faced by the Lagrangian stochastic modelling in the context of RANS. The picture becomes more optimistic when it comes to using the Lagrangian stochastic modelling to account for inertial particle transport by the sub-grid motion for LES. Indeed the temporally and spatially narrow range of the small scales that are discarded by the filtering in LES are deemed to be quasi isotropic and homogeneous. Thus, the model is expected to reproduce them with a higher degree of accuracy.

The Langevin-type stochastic process in the framework of LES was first used by Shotorban and Mashayek (2006) to model SGS transport of inertial particles in a decaying isotropic turbulent flow. However, particle inertia and cross trajectory effects were neglected which is valid only for inertial particles with vanishing response times. A detailed derivation of the Langevin-type stochastic process in the framework of LES of inhomogeneous and anisotropic turbulent flows was given by Berrouk et al. (2007), in which both inertia and cross trajectory effects were taken into account. Very promising results were obtained for the study of dispersion of particles with very small response times in a high-Reynolds turbulent pipe flow.

In this work, liquid particle deposition in a circular-sectioned 90° bend is numerically investigated using a well-resolved LES along with the Langevin-type stochastic model described in Berrouk et al. (2007). A well-resolved
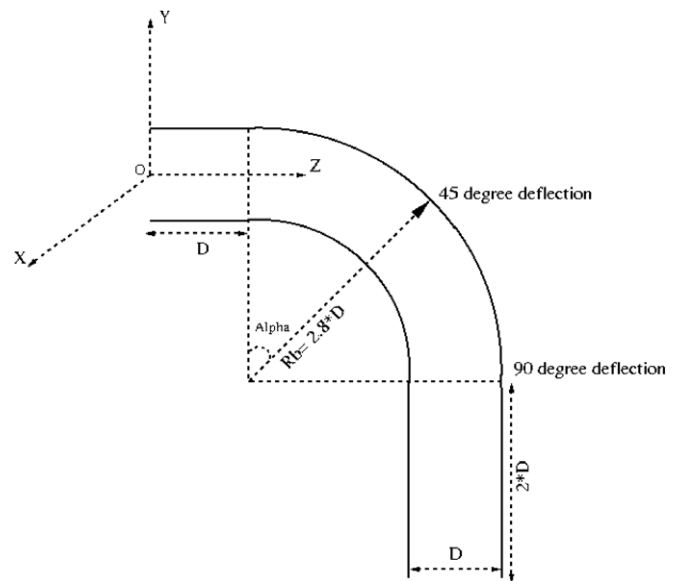


Fig. 1. External sketch of the circular-sectioned 90° bend.

LES is an LES where a portion of the relevant or energy-containing scales are not resolved. These discarded scales should not contain more than 25% of the kinetic energy according to Celik et al. (2003) and Pope (2004). The numerical predictions are compared to the experimental observations of Pui et al. (1987) and the fully-resolved LES results of Breuer et al. (2006). A fully-resolved LES is an LES where all the relevant or energy-containing scales are resolved. In the experimental work of Pui et al. (1987), the deposition efficiency of liquid particle in tube bend of circular cross-section was measured. Fig. 1 represents an external sketch of the circular-sectioned 90° bend while the experimental data are summarized in Table 1. The full description of the test facility, working parameters and data processing are given by Pui et al. (1987).

In fact the present numerical investigation is similar to the work of Breuer et al. (2006) with a major difference that it used a coarser numerical description. According to Breuer et al. (2006) the space resolution used in their work is found sufficient to resolve all relevant scales. In the present study a coarser description is adopted to allow certain amount of kinetic energy to be filtered out and a portion of the energetic small scales to be discarded. Such situation presents us with the opportunity to test the ability of the

Table 1
Experimental data

| | |
|---|---|
| Bend diameter | $D = 0.02$ m |
| Radius of curvature of the bend | $R_b = 0.056$ m |
| Curvature ratio | $R_0 = 5.6$ |
| Maximal velocity | $U \approx 10$ m/s |
| Reynolds number | $Re \approx 10,000$ |
| Dean number | $De \approx 4,225$ |
| Stokes number | $0.001 \leqslant St \leqslant 1.5$ |
| Particle density | $\rho_p = 895$ kg/m³ |

stochastic model to include sub-grid motion in the study of aerosol deposition.

## 2. Governing equations of particle-gas turbulent flow

### 2.1. Continuous phase

#### 2.1.1. Flow dynamics

In finite bends of circular cross-section, the turbulent flow dynamics is complex. Indeed it is characterized by the existence of recirculating regions and curved streamlines. For curvature ratio $R_0$ greater than five, the flow field in bends of circular cross-section depends only on the Dean number (Berger et al., 1983). The Dean number is defined as the flow Reynolds number divided by the square root of the curvature ratio:

$$De = Re \Big/ \sqrt{R_0}. \tag{1}$$

It represents the ratio of the square root of the product of centrifugal and inertial forces to the viscous forces. It plays the role of the Reynolds number of the flow in a curved pipe. The curvature ratio is defined as $R_0 = R_b/R$ where $R_b$ is the radius of curvature of the bend and R is the tube radius.

For high Dean number ($De > 370$) turbulent flow, secondary boundary layers develop on the wall, with fluid entering these boundary layers near the outer bend and leaving near the inner bend. A further increase of the Dean number, and hence the centrifugal force, leads to an increase in the axial velocity and to more fluid being sucked into the secondary boundary layers near the outer bend. The secondary boundary layers adjust by thinning near the outer bend and thickening near the inner bend. Simultaneously, the locations of the maximum axial velocity moves toward the outer bend. As a result of that, a symmetrical pair of counter-rotating helical vortices is formed.

These dynamical features that characterize a turbulent flow in a circular bend are expected to be captured by solving the Navier-Stokes equations for all the scales down to Kolmogorov scales. This is the direct numerical simulation and it is an expensive approach. LES is a practical alternative that relies on solving the anisotropic flow-dependent large scales while modelling the quasi homogeneous and isotropic small scales.

#### 2.1.2. Governing equations

LES formulation for the continuous phase is based on spatially filtering continuity and Navier-Stokes equations that describe the spatial and temporal evolution of fluid flows. In the case of an isothermal, incompressible and Newtonian fluid, they can be written as the following:

$$\frac{\partial \bar{u}_i}{\partial x_i} = 0, \tag{2}$$

$$\frac{\partial \bar{u}_i}{\partial t} + \frac{\partial \bar{u}_i \bar{u}_j}{\partial x_j} = -\frac{\partial \bar{p}}{\partial x_i} + \frac{1}{Re_\tau} \frac{\partial^2 \bar{u}_i}{\partial x_j \partial x_j} + \frac{\partial \tau_{ij}}{\partial x_j}, \tag{3}$$

where

$$\tau_{ij} = \bar{u}_i \bar{u}_j - \overline{u_i u_j}. \tag{4}$$

Here $Re_\tau$ is the Reynolds number based on the friction velocity $u_\tau$ and $\tau_{ij}$ is the sub-grid scale (SGS) stress tensor. It is modelled using the algebraic eddy-viscosity model proposed by Smagorinsky (1963):

$$\tau_{ij} - \frac{1}{3}\delta_{ij}\tau_{kk} = -2v_{SGS}\overline{S}_{ij}, \tag{5}$$

with $v_{SGS}$ is the sub-grid scale viscosity:

$$v_{SGS} = (C_s\Delta)^2 \left[1 - exp\left(-\frac{y^+}{A^+}\right)^3\right] |\overline{S}|. \tag{6}$$

Here $C_s$ is the Smagorinsky constant, its value is taken equal to 0.065. $|\overline{S}| = |2\overline{S}_{ij}\overline{S}_{ij}|^{1/2}$, where $\overline{S}_{ij} = \frac{1}{2}(\partial_j \bar{u}_i + \partial_i \bar{u}_j)$ is the resolved rate-of-strain tensor. The filter width $\Delta$ is taken equal to $2h$, where $h$ is the grid spacing $(h = (h_x.h_y.h_z)^{1/3})$. $\left[1 - exp\left(-\frac{y^+}{A^+}\right)^3\right]$ is a Van Driest damping function that accounts for the reduction of the sub-grid length near solid walls. It is based on the dimensionless distance from the wall $y^+ = yu_\tau/v$. $A^+$ is taken equal to 25. The filter width $\Delta$ used in the present LES is twice as wide as the filter used by Breuer et al. (2006) for their fully-resolved LES. For the choice of the Smagorinsky constant $C_s$, results of LES of channel and pipe turbulent flows performed using Code_Saturne have shown that the value of Smagorinsky constant that gives the closest estimations to the DNS results is $C_s = 0.065$ (Archambeau et al., 2004; Laurence, 2006).

Previous simulations of fully developed straight and curved pipe flow with the Smagorinsky model and the Van Driest damping function have shown good agreement with experiments (Boersma and Nieuwstadt, 1996; Berrouk et al., 2007). From turbulence modelling we know that RANS models based on eddy viscosity assumptions do not perform well in flows with curved streamlines. However in an LES, the Smagorinsky sub-grid model is only introduced to represent small scale dissipation and indeed, Eggels and Nieuwstadt (1993) showed that it correctly predicts the large scales in a rotating pipe flow.

The time step $\Delta t$ in the numerical simulations is taken equal to $0.1T$ where $T$ is the integral time scale defined as the ratio of the tube radius R and the velocity at the centre of the pipe $U_0$. This time step allows to hold the CFL number below 1.5 everywhere in the computational domain.

#### 2.1.3. Boundary conditions

To eliminate the unknown influence of the inlet and exit conditions on the flow development in the bend, a horizontal inlet section of length D is mounted to the 90° bend. The outlet is elongated by adding a vertical straight pipe with a length of 2D.

To avoid the use of artificial inflow data which often only partially satisfy all physical requirements, an appropriate inflow boundary conditions for the turbulent flow

within the bend is needed. For that purpose, a separate LES prediction of a 5D length straight pipe with the same cross-section, flow Reynolds number and time step size was carried out. Periodic conditions are used and the length of the straight pipe (5D) allows all the two-point correlations to vanish midway between the boundaries. When the turbulent pipe flow reaches a fully developed state, the velocity profile of one cross-section of this periodic LES is used as inflow conditions at the inlet of the pipe mounted in front of the bend.

Non-reflecting boundary conditions are applied at the outlet of the elongated bend. This ensures that all vortical structures can leave the integration domain without significant disturbances or wave reflections into the inner region. Since the first grid point is placed sufficiently close to the wall, it is possible to apply the no-slip boundary condition at the wall. The pressure is computed assuming a vanishing pressure gradient in the wall-normal direction.

### 2.1.4. Grid resolution

An unstructured grid consisting of 1,300,000 cells is used with about 4,700 grid points on each cross-section. A polar grid is used for the first three layers with non-conforming embedded refinement as shown in Table 2. Then the polar grid is made to match an octahedral block for the core region as it is depicted in Fig. 2. The first grid point near the pipe wall at which the axial velocity is computed is located at $y^+ \approx 1.3$, with 3 grid points placed within the viscous sublayer, the depth of which equals 5 wall units. A non-uniform grid is employed in the normal-to-the-wall direction within the circular part. This is done in order to locate more grid points in the near-wall region. It is worth noting that two grid points in the viscous sublayer is in general enough for LES of straight pipe flow. For curved pipe the thickness of the viscous sublayer is non-uniform. Indeed for the fully developed curved pipe, the sublayer thickness at the outside radius is approximately 3.5 wall units while at the inside radius the depth of the viscous layer measures 8 wall units. By having 3 points under 5 wall units everywhere in the domain, the resolution of the viscous sublayer regardless its location should be adequate especially at the outside of the bend. It is also clear that the resolution at the inside of the bend and in the straight pipes will be increased since more than 2 points are used to resolve the viscous sublayer.

Care should be taken when using the non-conforming embedded refinement to locate more cells where resolution
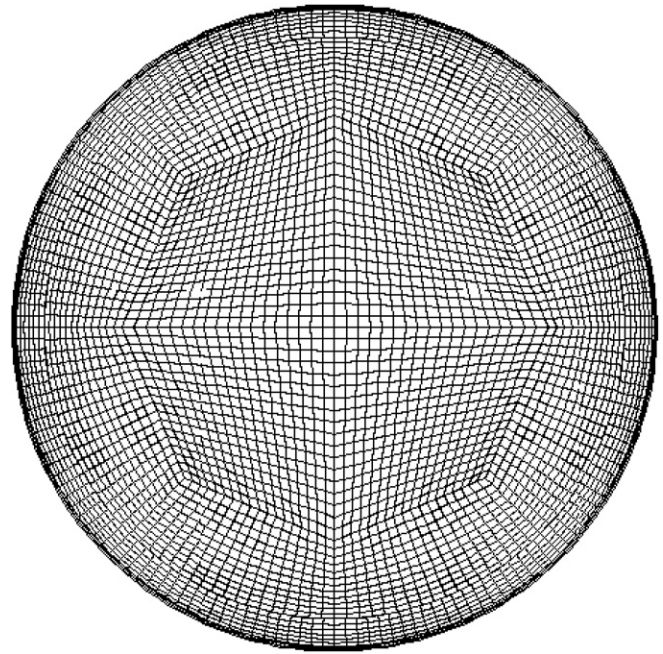


Fig. 2. Use of non-conforming embedded refinement for LES grid.

is needed. The near-wall region is characterized by steep gradients and very small energy-containing eddies that should be well captured. These near-wall coherent structures contain most of the turbulence and are responsible for the correct distribution of the turbulent energy from the streamwise into the other directions. Moreover, the near-wall turbulence has a significant impact on the deposition of inertial particles and therefore it should be properly resolved. As depicted in Fig. 2, the different non-conforming layers are designed such that the aspect ratios between the cell sizes in the different directions do not exceed 5 to avoid numerical instabilities that arise when using very flat cells. Thus the use of non-conforming layers should be efficient since it allows a cell distribution that responds to the requirement of the flow dynamics without introducing further numerical errors.

The LES calculations performed by Breuer et al. (2006) for the same case used a grid that consisted of 2,280,000 cells with 8,900 grid points in each cross-section. According to Breuer et al. (2006) the resolution is found sufficient to resolve all relevant scales at the moderate Reynolds number considered in the present study. However, no evidence was given to underpin their claim such as an estimation of the amount of the filtered-out kinetic energy.

The unstructured grid used in the present LES appears to have a similar number of grid points to the block-structured grid used by Breuer et al. (2006) but the distribution of cells in all the directions is very different. Indeed, Breuer's grid is finer than the present LES grid in the near wall layer (with the first point near the wall at $y^+ = 0.35$ while in the present LES the first point is at $y^+ = 1.3$). For the streamwise direction, Breuer used 257 grid points while for the present LES, 240 grid points were used in the core

Table 2
Non-conforming embedded refinement in the polar part of the unstructured grid

| $Y^+ = u_\tau \cdot y / v$ | Rad. direction | Circumf. direction | Streamwise direction |
|---|---|---|---|
| $0 < y^+ < 5$ | 3 cells | 240 cells | 400 cells |
| $5 < y^+ < 30$ | 6 cells | 168 cells | 360 cells |
| $30 < y^+ < \approx 180$ | 12 cells | 144 cells | 240 cells |

region then the number of grid points in the streamwise direction was increased with increasing radius to reach 400 grid points in the vicinity of the wall (see Table 2.). This, in order to keep the aspect ratio between the radial and streamwise direction under 5.

Concerning the cross-section, Breuer's discretisation is finer in the circumferential direction, but accounting for the unstructured nature of the present grid, the difference between Breuer's grid (8900 cells in cross section) and the present one (4700 cells) is not very large when individual cell sizes are compared.

Finally, in the present LES all the governing equations of the two phases were solved in the physical space while in Breuer et al. (2006) a coordinate transformation was used to solve the governing equations in a so-called computational space.

## 2.2. Dispersed phase

### 2.2.1. Governing equations

Aerosols are released and tracked in the turbulent flow that is described in the previous section. The physical properties of these inertial particles are summarized in Table 3.

As a result of the high density ratio between particle and fluid densities, the equation describing particle motion is reasonably simple and only the drag and gravity forces will be retained since other forces are in this case negligible (Maxey and Riley, 1983). The tracking of the inertial particles within the turbulent flow obeys the following system of equations:

$$dx_{p,i} = u_{p,i}dt,$$

$$du_{p,i} = \frac{u_{p,i} - u_{s,i}}{\tau_p}dt - g_i dt,$$

$$\tau_p = C_n \frac{\rho_p}{\rho_f} \frac{4d_p}{3C_D|u_s - u_p|}, \qquad (7)$$

$$C_D = \begin{cases} \frac{24}{Re_p}(1 + 0.15Re_p^{0.687}) & \text{if } Re_p < 1000 \\ 0.44 & \text{if } Re_p > 1000. \end{cases}$$

Table 3
Physical characteristics of the tracked inertial particles

| Mean diameter $d_p(\mu m)$ | Cunningham factor $C_n$ | Response time $\tau_p$(ms) | Stokes number St |
|---|---|---|---|
| 0.62 | 1.280 | 0.0011 | 0.001 |
| 4.77 | 1.042 | 0.055 | 0.05 |
| 6.80 | 1.024 | 0.11 | 0.1 |
| 9.65 | 1.019 | 0.22 | 0.2 |
| 11.23 | 1.015 | 0.29 | 0.27 |
| 11.64 | 1.015 | 0.32 | 0.29 |
| 14.70 | 1.007 | 0.5 | 0.46 |
| 18.83 | 1.003 | 0.82 | 0.75 |
| 19.95 | 1 | 0.92 | 0.84 |
| 21.77 | 1 | 1.09 | 1 |
| 24.05 | 1 | 1.33 | 1.22 |
| 25.30 | 1 | 1.47 | 1.35 |
| 26.66 | 1 | 1.64 | 1.5 |

Here $x_p$ and $u_P$ are the particle position and velocity, $u_s$ is the fluid velocity seen by an inertial particle along its trajectory, $g$ is the gravity force per unit of mass, $d_p$ and $\rho_p$ are the diameter and the mass density of inertial particles, $\tau_p$ is the particle response time, $C_D$ is the drag coefficient and $Re_p$ is the particle Reynolds number, $Re_p = d_p |u_s - u_p|/v$ with $v$ is the kinematic fluid viscosity. $C_n$ is Cunnigham slip correction factor. It is considered herein to correct the drag coefficient in order to take into account the free-slip boundary conditions that occur at the surface of the particles.

To ensure particle statistics of high quality, the number of released particles was set to a reasonably large value; 250,000 particles in order to reduce the statistical noise on the deposition results. These particles are randomly distributed over the cross-section at the inlet. They are all released at the first time step and then tracked throughout the flow field until they exit the bend or deposit on the wall.

It is considered that particles adhere to the surface upon contact. Numerically, contact is supposed to occur when the particle radius is smaller or equal to the normal distance between the surface and the particle centre. No bounce from the surface is considered. Though a large number of particles are released and tracked within the flow, neither two-way coupling nor particle collision are considered. This is consistent with the experimental work of Pui et al. (1983) since they used a very dilute suspension. A trilinear interpolation scheme is used to obtain the velocities between the grid points.

The only unknown in the system of Eq. (7) is the fluid velocity $u_s$ seen by inertial particles along their trajectories as they move through the turbulent field. The Eulerian velocity field described in Section 2.1 contains only part of the information of the velocity field that inertial particles should see. This information is linked to the filtered velocity of the large scales. Any information about the sub-grid scale motion is lost because of the filtering operation. As it was explained in the introduction, this information about the turbulence at the sub-grid scale level is crucial for the transport of inertial particles with response times smaller than the smallest LES-resolved time scales.

In the next section, the Langevin-type stochastic model proposed by Berrouk et al. (2007) is used to reconstruct the Lagrangian instantaneous fluid velocity seen by inertial particles based on the LES filtered velocity field. This model accounts for the inertial character of the particles and the presence of a body force.

### 2.2.2. Modelling of the fluid velocity seen by the particles

The general form of the Langevin model chosen for the velocity of the fluid seen by particles is:

$$du_{s,i} = A_{s,i}(t, x_p, u_p, u_s)dt + B_{s,ij}(t, x_p, u_p, u_s)dW_j, \qquad (8)$$

where the drift vector A and the diffusion matrix B have to be modeled. Each component of the vector dW is a Wiener process (white noise); it is a stochastic process of zero mean, $\langle dW \rangle = 0$, a variance equal to the time interval,

$<(dW)^2> = dt$, and delta-correlated in the time domain (Kloeden and Platen, 1999).

The theoretical and numerical formulations of the Langevin model have been extensively discussed in the framework of particle-laden RANS by Pozorski and Minier (1998) and Minier et al. (2003). The use of the Langevin model is extended by Shotorban and Mashayek (2006) and Berrouk et al. (2007) with the necessary modifications for the modelling of time increment of the fluid velocity seen by inertial particles in LES framework. A detailed derivation of the different terms of the Lagrangian model is provided by Berrouk et al. (2007). Herein, only the evaluation of these terms in the case of inhomogeneous and anisotropic turbulence and how inertia and CT effects are accounted for is provided. The Langevin-type model reads:

$$du_{s,i} = \left(-\frac{1}{\rho_f}\frac{\partial \bar{p}}{\partial x_i} + \frac{1}{Re}\frac{\partial^2 \bar{u}_i}{\partial x_j \partial x_j}\right)dt - \left(\frac{(u_{s,i} - \bar{u}_i)}{T_{SGS}^*}\right)dt + \sqrt{C_0^* \langle \epsilon_r \rangle}dW_i. \tag{9}$$

Here $u_s$ is the fluid velocity seen by particles along their trajectories, $T_{SGS}^*$ is the fluid SGS time scale seen by particles, $C_0^*$ is the diffusion constant and $<\epsilon_r>$ is the dissipation rate of the SGS kinetic energy $k_{SGS}$. The fluid SGS time scale seen by inertial particles $T_{SGS}^*$ is $T_{E,SGS}$ (the Eulerian SGS time scale) in the limit of large Stokes number. On the other hand, $T_{SGS}^* = T_{L,SGS}$ (the Lagrangian SGS time scale) if $St \to 0$ since in this case the inertial particles reduce to fluid elements. Thus, $T_{SGS}^*$ in general is a function of St and varies between $T_{L,SGS}$ and $T_{E,SGS}$ as it is portrayed in the following equation (Wang and Stock, 1993):

$$T_{SGS}^* = \frac{T_{L,SGS}}{\beta}\left(1 - (1 - \beta)(1 + St)^{-0.4(1 + 0.01St)}\right). \tag{10}$$

St is Stokes number based on the Eulerian SGS time scale and $\beta$ is the ratio between the Lagrangian and the Eulerian time scales. It is assumed that $\beta$ keeps the same value across the different scales of turbulence:

$$\beta = T_L/T_E = T_{L,SGS}/T_{E,SGS}. \tag{11}$$

It was shown that its value is Reynolds number dependent (Sato and Yamamoto, 1987) and varies considerably in the literature. For this study, it is expected that its influence on the model predictions is very small, since small universal scales are modeled. In this study, $\beta$ is chosen to be 0.356 (Wang and Stock, 1993).

Eq. (10) was developed for particles interacting with homogeneous and isotropic turbulence. Its use in the present context to account for inertia effect on Lagrangian sub-grid time scale is more appropriate compared to its use to include inertia effect on Lagrangian time scale in the framework of RANS/SM where the construction of a wide spectrum of anisotropic turbulence fluctuations is sought through the stochastic modelling.

For LES, the Lagrangian time scale for the sub-grid fluctuations $T_{L,SGS}$ is computed using the sub-grid kinetic energy $k_{SGS}$ and its dissipation rate $\epsilon_r$ that have to be evaluated according to the SGS model used to take into account sub-grid effects on the large scales. It reads following Heinz (2003):

$$T_{L,SGS} = \left(\frac{1}{2} + \frac{3}{4}C_0\right)^{-1}\frac{k_{SGS}}{\langle \epsilon_r \rangle}. \tag{12}$$

In the case of the Smagorinsky model, if equilibrium is assumed at the cut-off, the production balances the dissipation. Thus, the SGS kinetic energy and its dissipation rate can be evaluated as:

$$\epsilon_r = -\tau_{ij}.\frac{d\bar{u}_i}{dx_j} = (C_s.\Delta)^2|\bar{S}|^3, \tag{13}$$

$$k_{SGS} = C_\epsilon(\Delta.\epsilon_r)^{2/3}. \tag{14}$$

Typically $C_\epsilon \sim 1$ and $C_0 \sim 2.1$ (Gicquel et al., 2002).

The directional dependence of the fluid Lagrangian SGS time scales $T_{L,SGS}$ is neglected since sub-grid scales are assumed to be homogeneous and isotropic.

To account for the cross trajectory effect due to the presence of a body force, the Lagrangian time scale is expressed in the case of inertial particle as function of the instantaneous relative velocity between the fluid and the inertial particles. Since there is a difference between the longitudinal and transverse length scales for the spatial correlations, it is important to have a non isotropic form for $T_{SGS}^*$. To achieve this purpose, it is important to distinguish between the time scale measured in the direction of the mean relative velocity and the time scale measured in the transversal direction. If the direction (1) is aligned with the direction of the mean relative velocity and (2) and (3) are the transversal ones, we can use Csanady formulas (Csanady, 1963) to compute the different anisotropic time scales:

$$T_{SGS,\parallel}^* = \frac{T_{SGS}^*}{\sqrt{1 + \beta^2 \mid \langle u_r \rangle \mid^2/(2k/3)}},$$

$$T_{SGS,\perp}^* = \frac{T_{SGS}^*}{\sqrt{1 + 4\beta^2 \mid \langle u_r \rangle \mid^2/(2k/3)}}. \tag{15}$$

Here $\langle u_r \rangle$ is the mean slip velocity between fluid and inertial particles. $k$ is the resolved turbulent kinetic energy. In fact Csanady formulas also take into account the continuity effect. The continuity effect postulates that the inertial particle dispersion in a direction perpendicular to the mean drift is twice as faster as inertial particle dispersion in a direction parallel to the mean drift.

The diffusion coefficient $C_0^*$ is evaluated according to the following formulation (Minier and Peirano, 2001):

$$C_0^* = C_0 b_i \tilde{k}_{SGS}/k_{SGS} + \frac{2}{3}(b_i \tilde{k}_{SGS}/k_{SGS} - 1), \tag{16}$$

where $C_0$ is the Kolmogorov constant, and $\tilde{k}_{SGS}$ is a modified SGS kinetic energy:

$$\tilde{k}_{SGS} = \frac{3}{2} \frac{\sum_{i=1}^{3} b_i < u'^2_i >}{\sum_{i=1}^{3} b_i} \tag{17}$$

Here $u'_i$ is the fluid fluctuating velocity and $b_i = T^*_{SGS}/T^*_{SGS,i}$ ($i = \perp$ or $\parallel$).

At each time step $\Delta t$, Eqs. (10)–(17) are evaluated for each particle separately. The stochastic differential equations (SDE) system that comprises Eqs. (7) and (9) is integrated using an appropriate weak second-order integration scheme (Minier et al., 2003) that accounts for the nature of the problem characterized by the presence of different time scales; this can lead to stiff equations when the smallest time-scale is significantly less than the time-step of the simulation. This point is crucial for physical and engineering applications, where various limiting cases can be present at the same time in different parts of the domain or at different times. Because turbulence problem has a multi-scale character, three time scales are considered: The observation time scale, $\Delta t$, and two physical time scales, the particle relaxation time, $\tau_p$, and the time scale of the fluid velocity seen, $T^*_{SGS}$. When these scales go to zero, a hierarchy of stochastic differential systems is obtained. The Langevin-type model used in this study degenerates to a stochastic model for turbulent diffusion when $\tau_p \to 0$, that is, the inertial particles behave like fluid particles.

The weak second-order integration scheme consists of a prediction step and a correction step. The prediction step is a weak first-order integration scheme (Euler scheme). By freezing the coefficients on the integration intervals and by resorting to Ito's calculus, it can be shown that the above SDE system has an analytical solution. The analytical solutions for particle position $x_p$, velocity $u_p$ and seen fluid velocity $u_s$ are given in Appendix.

As it was highlighted by MacInnes and Bracco (1992) and Minier and Peirano (2001), the Langevin model under the formulation (9) does not suffer any spurious drift in the non-homogeneous case.

## 2.3. Flow solver

A flow solver from the R&D section of Electricite de France named Code_Saturne was used as starting point of the present development. The discretization in Code_Saturne is based on the collocated finite-volume approach. It allows solving Navier-Stokes and scalar equations on hybrid and non-conform unstructured grids. Velocity and pressure coupling is ensured by a prediction/correction method with a SIMPLEC algorithm. The collocated discretization requires a Rhie and Chow interpolation in the correction step to avoid oscillatory solutions. A second order centred scheme (in space and time) is used. The flow solver has been extensively tested for LES of single-phase flows (Archambeau et al., 2004; Laurence, 2006) as well as its Lagrangian module for particle tracking based on RANS/stochastic modelling (Minier et al., 2004).

## 3. Results and discussions

### 3.1. Continuous phase

The continuous flow field in the circular bend is simulated using LES as it is described in Section 2.1. Fig. 3 shows the pressure field and the time-averaged velocity in the symmetry plane ($x = 0$). Fig. 4a shows a LES instantaneous velocity field at a randomly chosen instant. Secondary streamlines are presented in Fig. 4b. For comparison, instantaneous velocity field and secondary streamlines of Breuer et al. (2006) work are presented in Fig. 5.

As the fluid flows through the straight pipe and redirected into a bend the pressure which in the straight section is uniform across the flow, must adjust in the bend to counter centrifugal forces. The pressure is greatest at the outer wall farthest from the centre of curvature and least at the inner wall nearest to the centre of curvature. At the bend inlet the negative pressure gradient on the inner wall is approximately twice the positive gradient on the outside as it is depicted in Fig. 6. These initial gradients resulting
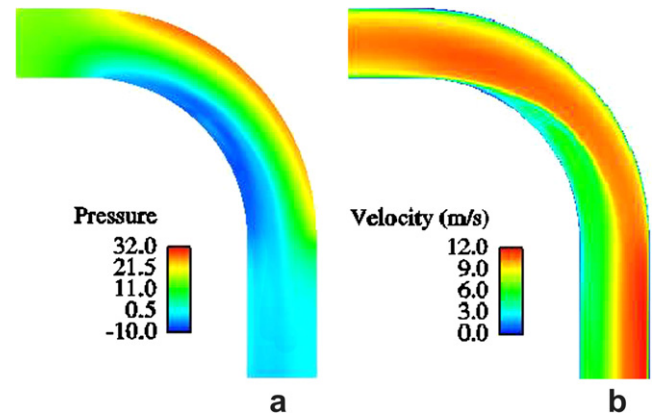


Fig. 3. LES predictions of the turbulent flow in the mid-plane of the bend. (a) Pressure field of the time-averaged flow, (b) velocity magnitude of the time-averaged flow.
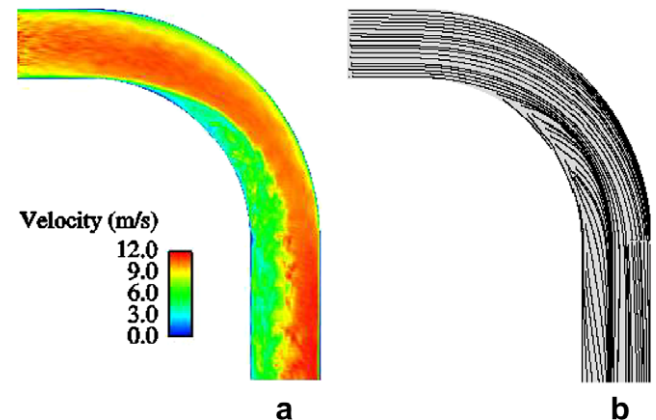


Fig. 4. LES predictions of the turbulent flow in the mid-plane of the bend. (a) Velocity magnitude of the instantaneous flow, (b) streamlines of the time-averaged flow.

from the change from straight to curved flow disappear at approximately *alpha* = 20° (see Fig. 1 for the definition of angle of deflection *alpha*) so that in the mid section of the bend between *alpha* = 20° and *alpha* = 80° a quasi equilibrium condition is reached with approximately uniform pressure on the inner and outer walls. The cross-stream pressure gradient established in the bend as it is depicted in Fig. 3a has well known effects on the flow. At the bend inlet, the boundary layer on the outer wall experiences the effect of an adverse streamwise pressure gradient which may in a tight bend be sufficiently strong to produce local separation, conversely at the inner wall the boundary layer is accelerated. The reverse occurs at the pipe exit where local pressure gradients of the opposite sign appear as the flow adjusts to uniform pressure conditions downstream.

The impact of the curved geometry into the straight section usually extends some distance upstream of the bend as it is shown in Figs. 3b and 4a. Therefore the resulting flow at the entrance of the bend already differs considerably from of a fully developed pipe flow and should affect the secondary flow patterns within the bend as we shall discuss below.

The streamlines in the plane of symmetry as predicted by LES calculations are presented in Fig. 4b. They provide an indication of the secondary flow in the bend. The present well-resolved LES results for the instantaneous velocity field and streamlines compare fairly well with the predictions of the fully-resolved LES of Breuer et al. (2006) as portrayed in Fig. 5.

The flow in a bend is influenced by centrifugal force due to the curvature. This centrifugal force is, in principle, balanced by a pressure gradient in the plane of curvature. However, near the wall where the velocity is small, this pressure gradient can no longer be balanced and consequently the fluid in the middle of the pipe moves outward and impinges on the outer wall and then turns to move inward along the wall to merge at the inner wall. This flow impingement on the outer wall and separation at the inner wall make flows in curved pipe whether laminar or turbulent very complex. The result is a secondary flow superimposed on the main flow in the plane perpendicular to the mean flow. The magnitude and the shape of this secondary motion depend on the Dean number.

The direct effect of the secondary flow is to displace the region of maximum velocity from the centre towards the outer wall as it is shown in Fig. 7. For the bend entrance, the mean axial velocity profile is significantly altered with respect to the fully developed profile in the straight pipe and the location of the maximum velocity is shifted toward the inner bend (I) as it is depicted in Fig. 7a. This is
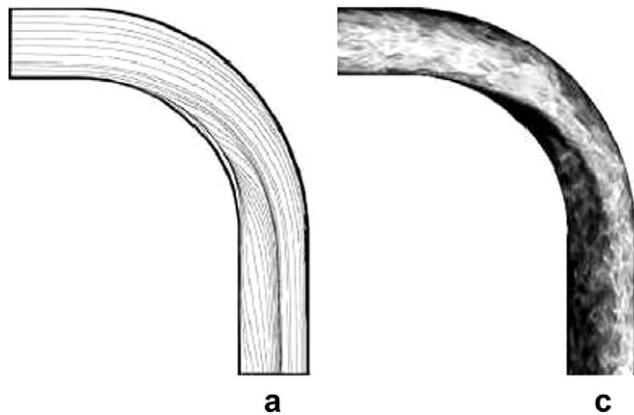


Fig. 5. Breuer et al. (2006) predictions of the turbulent flow in the mid-plane of the bend. (a) streamlines of the mean flow, (c) velocity magnitude of the instantaneous flow.
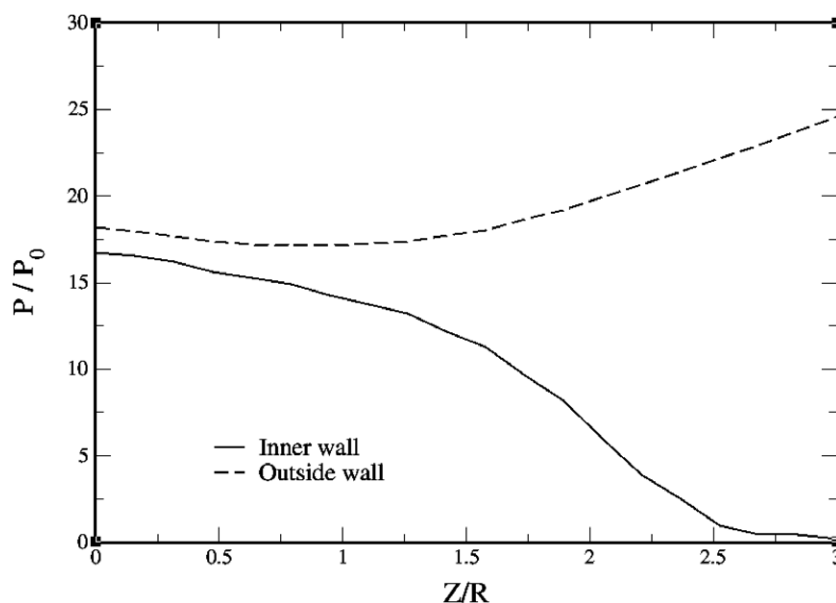


Fig. 6. LES predictions of the pressure field near the wall at the bend entrance. $P_0$ is the reference pressure.
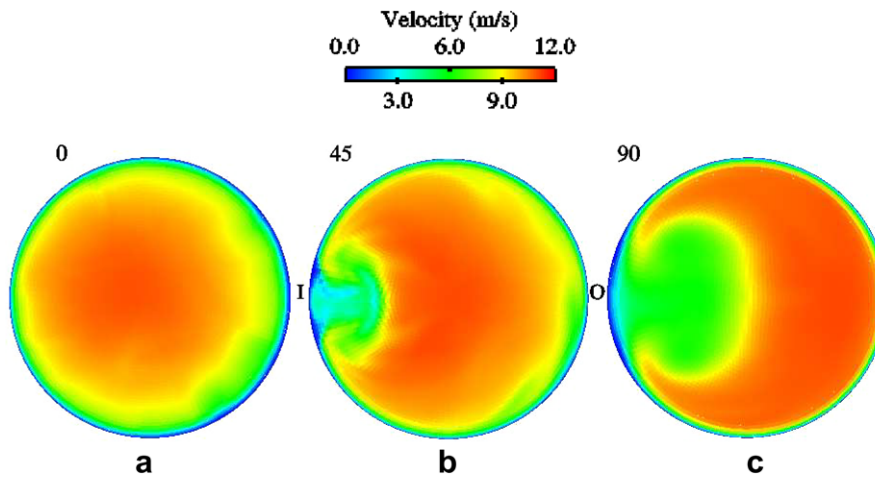
Fig. 7. LES predictions of mean axial velocity in different sections of the bend. (a) Bend entrance, (b) 45° deflection, (c) 90° deflection. See Fig. 1 for the definition of angle of deflection alpha.

explained by the fact that no centrifugal forces due to the redirection of the flow are present at the bend entrance, but the radial pressure gradient of the curved section is already perceptible which induces a secondary flow directed to the inner side over the entire cross-section.

The flow in 90° bends is almost always developing flows, in which the velocity distributions do not attain forms that are independent of the position along the pipe axis. Fig. 7b and c show the cross-section mean axial velocity as it develops downstream the bend entrance at 45° and 90° deflections.

At 45° deflection the outward movement of the location of the maximum axial velocity is evident in LES results with a perceptible thickening of the secondary boundary layer and zone of flow recirculation around the innermost of the bend. At the bend exit, the time-averaged axial velocity moves further toward the outer radius and the bound-

ary layer is uniformly thick on the inner bend while becoming thinner on the outer radius. These trends are also visible in Fig. 8 depicting the mean axial velocity profile within the bend.

The secondary motion can be seen more clearly by observing the mean streamlines in cross-sections as it is depicted in Figs. 9 and 10 for the present LES and the work of Breuer et al. (2006) respectively. At the bend entrance and as mentioned earlier the centrifugal forces are very weak to balance the pressure gradient which results in an inward flow as it is shown in Fig. 9a. With increasing deflection, the centrifugal forces increase and the time-averaged flow fields show the well known counter-rotating Dean vortices that circulate in the outward direction in the central part of the pipe, which is the opposite direction compared with the bend entry. This is depicted in Fig. 9 for the 45° deflection. Moreover, an additional secondary flow
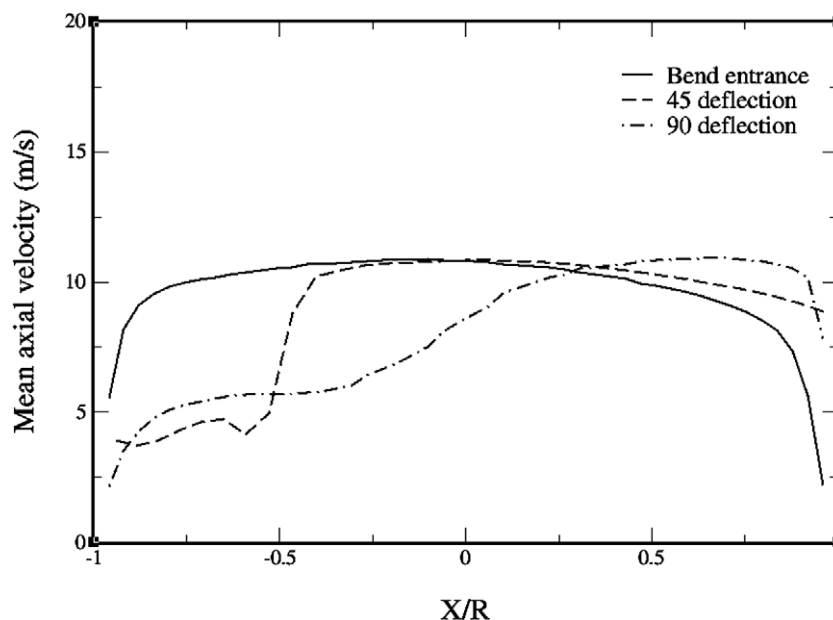


Fig. 8. LES predictions of the mean axial velocity profile for different cross-sections of the bend.
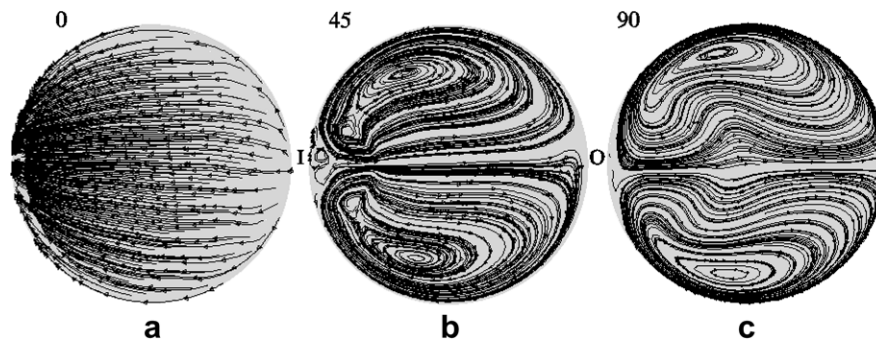
Fig. 9. LES predictions of the streamlines of the secondary flow in different sections of the bend. (a) Bend entrance, (b) 45° deflection, (c) 90° deflection. See Fig. 1 for the definition of angle of deflection alpha.
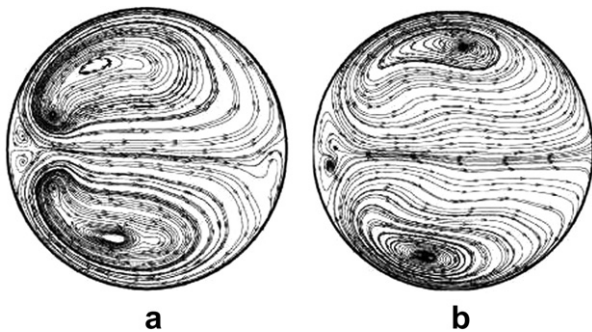


Fig. 10. Breuer et al. (2006) predictions of the streamlines of the secondary flow in different sections of the bend. (a) 45° deflection, (b) 90° deflection. See Fig. 1 for the definition of angle of deflection alpha.

structure consisting of a pair of small counter-rotating vortices is predicted by the present LES and visible at the inner radius in Fig. 9b. At higher deflection, the centre of these secondary vortices moves from the inner radius to the outer radius and get closer to the wall as it is shown in Fig. 9c for the present LES calculations. Predictions of the secondary motion for the present LES are compared with the results of Breuer et al. (2006) depicted in Fig. 10. Globally, good agreement is found except in the core region of the cross-section at 90° deflection where a more pronounced distortion of the secondary streamlines is noticed for the present LES, and the pair of the small counter-rotating vortices occurring at the inner radius is not visible in Fig. 9c. It is conjectured that they were not visible in Fig. 9c because of their small sizes but surely captured by the present LES. Indeed, they do exist in that region preventing particles from depositing at the inner-most radius of the bend as we shall discuss in the next section.

They are clearly some difference in the more minute details of the predicted flow fields, but prolonging the discussion is not useful in the absence of experimental data. Indeed, most of the experimental works investigated turbulent flows in curved bend of a very high Dean number, well beyond the Dean number of the test case in hand (Boersma and Nieuwstadt, 1996). For the few works where a comparable Dean number bend flows are studied, the curvature ratio turned out to be less than five. It is well known that in such cases the conditions of similarity between flows in curved bend depends on both Reynolds number and curvature ratio

and no longer on their combination, i.e., Dean number (Berger et al., 1983). Moreover, the work of Pui et al. (1983) does not provide any results about the continuous phase.

To assess *a-posteriori* the quality of the present LES results, the ratio of the sub-grid scale kinetic energy $k_{SGS}$ to the total kinetic energy $k$ is computed. Fig. 11 shows an estimation of this ratio in the different directions. This form of presentation gives an overall impression and was chosen since the flow in curved bend does not own a direction of statistical homogeneity. The SGS kinetic energy is estimated using Eqs. (13) and (14). In X direction and thanks to the non-conforming embedded refinement near the wall, the filtered out kinetic energy is kept under 5% which means that the near-wall turbulence is well resolved. This has a positive repercussion on the prediction of particle deposition that is significantly influenced by the near-wall turbulence. Saying that, the amount of the kinetic energy filtered out at the near wall region, though small (around 5%), still corresponds to a range of small-scale turbulent fluctuations that could influence the transport of particles with very small Stokes numbers. Thus the use of the stochastic model is justified for both the near-wall region and the core region to well predict deposition and dispersion of inertial particles. In Y and Z directions, a ratio higher than 20% is noticed in the region $-3 < Y/R < -2$ and $5.5 < Y/R < 6.5$ which is the region around 45° deflection. In this region, the grid should be finer In order to keep the ratio around 20%.

Globally, the ratio of the SGS kinetic energy to the total kinetic energy is well under 20% almost everywhere in the domain and consequently the present LES is adequate according to the index of LES quality developed by Celik et al. (2003).

### 3.2. Dispersed phase

For the dispersed phase, the deposition efficiency is computed for different particle Stokes numbers using the following equation:

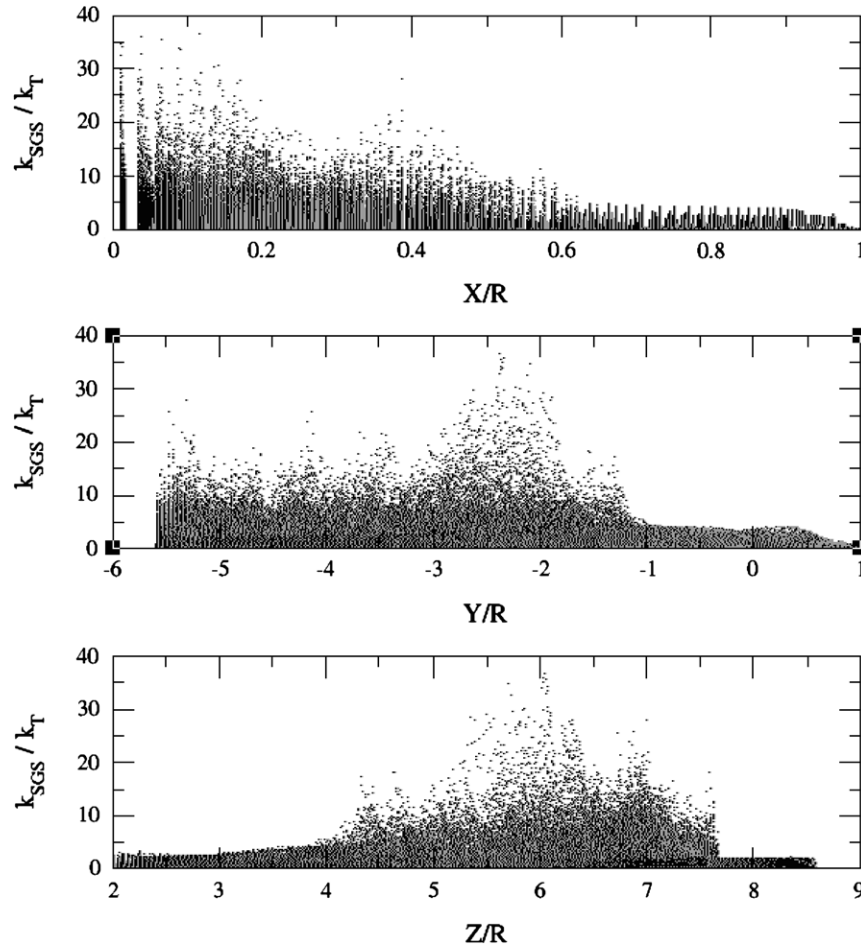$$\eta_p = \frac{N_p^{bend}}{N_p^{bend} + N_p^{after\ bend}}, \tag{18}$$

Fig. 11. Ratio of the sub-grid scale kinetic energy $k_{SGS}$ to the total kinetic energy $k$ in different directions.

where $N_p^{bend}$ is the number of particles that deposit in the bend and $N_p^{after\ bend}$ is the number of particles that exit the bend. The Stokes number of the liquid particles considered ranges from 0.001 to 1.5 as it shown in Table 3. This range of particle Stokes number covers a wide inertial particle behaviour toward the SGS turbulence present in the flow. For particles with small Stokes number ($St < 0.2$), it is expected that the sub-grid scale turbulence should have a significant impact on their transport and thus deposition. For particle with intermediate Stokes number ($0.2 < St < 1$), they should be more transported by the resolved turbulence with a possibility of SGS turbulence to influence particles with Stokes number at the lower end of this range. For the third category that contains particles with Stokes numbers equal or larger than 1, they will not sense the turbulence present in the flow and their inertial deposition will be affected by the mean flow. For these particles, LES using only the resolved field (no stochastic modelling) is therefore expected to predict well their deposition efficiencies.

Fig. 12 depicts LES results of the deposition efficiency in comparison with the measurements of Pui et al. (1983) and the numerical results of Breuer et al. (2006). Also, a curve fitted through the experimental data by Pui et al. (1983) is added which describes the deposition efficiency as a function of the Stokes number:

$$\eta_p = 1 - 10^{-0.963St}. \tag{19}$$

It is worthy to mention that relation (19) is a fit for the experimental observations of Pui et al. (1983) for particles with Stokes number between 0.27 and 1.35. Therefore, the curve is displayed in dashed line for $St < 0.27$.

The use of the filtered velocity field only to track the inertial particles with Stokes numbers higher than 0.5 shows good agreement with the experimental results of Pui et al. (1983) and the LES results of Breuer et al. (2006).

For particles with $St < 0.5$, the deposition is underestimated and the differences between the LES predictions using only the filtered velocity field and the results of both Breuer et al. (2006) and the present LES using the stochastic model become significant as the Stokes number becomes smaller. Table 4 summarizes the differences in deposition efficiencies $\eta_p$ predicted by the present LES with and without the stochastic model SM. These differences are computed as a ratio $D_1$ or as a percentage $D_2$:

$$D_1 = \eta_p(\text{with } SM)/\eta_p(\text{without } SM),$$
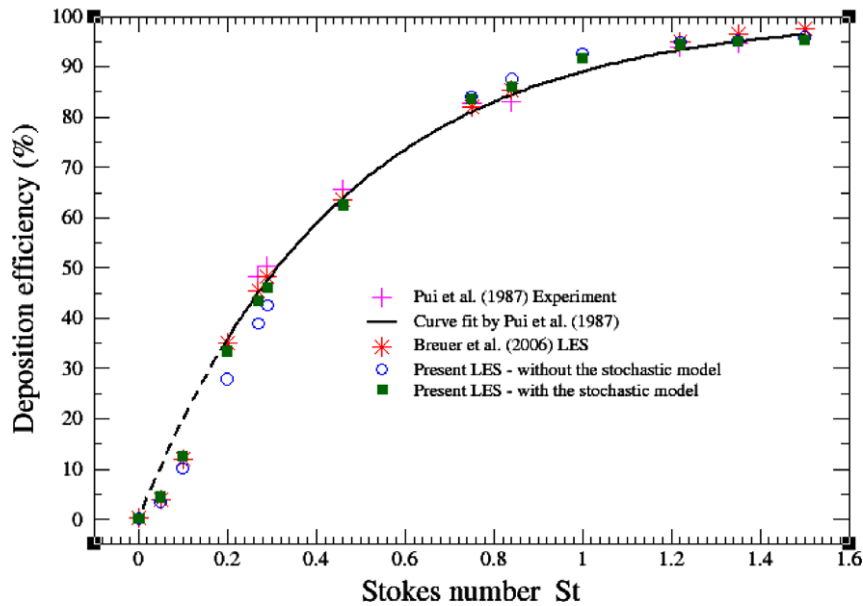$$D_2 = [\eta_p(\text{with } SM) - \eta_p(\text{without } SM)]/\eta_p(\text{with } SM)\%. \tag{20}$$

Fig. 12. LES predictions of deposition efficiency versus particle Stokes number. $St = \tau_p U_0/R$.

Table 4
Differences in deposition efficiencies predicted by LES with and without the stochastic model SM. $D_1$ and $D_2$ are computed using Eq. (20)

| St | Breuer et al. (2006) | Present LES without SM | Present LES with SM | $D_1$ | $D_2(\%)$ |
|---|---|---|---|---|---|
| 0.001 | 0.18 | 0.14 | 0.2 | 1.43 | 30 |
| 0.05 | 4 | 3.5 | 4.4 | 1.26 | 21.5 |
| 0.1 | 12 | 10.16 | 12.6 | 1.24 | 19.4 |
| 0.2 | 35 | 27.95 | 33.5 | 1.20 | 16.57 |
| 0.27 | 45.5 | 38.92 | 43.55 | 1.12 | 10.63 |
| 0.29 | 48.3 | 42.59 | 45.99 | 1.08 | 7.39 |

These differences in deposition efficiencies suggest that for particles with Stokes number less than 0.5, the large-scale turbulence fluctuations contained in the filtered LES velocity field are not solely responsible of their dispersion and deposition. For this class of particles, the discarded SGS turbulence should be taken into account in order to predict the correct level of turbulence these particles should see and thus the correct deposition efficiency. For particles with Stokes number higher than 0.5, the LES predictions of the deposition efficiency should be similar whether the SGS stochastic modelling is used or not because these particles simply do not sense the SGS turbulent fluctuations. Fig. 12 shows that this is the case and very good agreement with the reference results is found.

An estimation of the time scale of the SGS fluctuations that are washed out by the filtering operation in the present LES shows that the SGS motion should have an important role for the dispersion and deposition of part of the particles considered in theses simulations. Fig. 13 presents an estimation of the SGS time scales in the computational domain in different directions. The SGS time scale $T^*_{SGS}$ is non-dimensionalized by the integral time scale $T = R/U_0$ on which the particle Stokes number in Fig. 12 is based. This estimation is made according to Eq. (12). For the case

in hand the SGS time scale ranges between $0.12T$ and $0.25T$ and consequently particles with response times smaller than $0.25T$ will sense a portion or the whole turbulence linked to the SGS motion depending on their response times. This agrees well with the results of Fig. 12. Indeed a deviation between the deposition efficiency as predicted by LES using the filtered field and the reference results becomes noticeable for particles with a response time equals to $0.29T$ and become more significant as the Stokes number goes down as it is shown in Table 4.

The fluid velocity seen by the particles taking into account SGS fluctuations is constructed as it is described in Section 2.2.2. The present deposition efficiency predictions obtained by using the stochastic model confirm the results of the work of Breuer et al. (2006). There are some differences between the deposition efficiencies predicted by the present LES and those predicted by the work of Breuer et al. (2006) (see Table 4) and this is due to the existence of some discrepancies between the single-phase results of the two simulations as it was discussed in Section 3.1. It is worth mentioning that the evaluation of the different terms of the stochastic model is based on the different resolved variables of the single-phase flow (pressure and velocity fields, SGS kinetic energy and its dissipation rate and the SGS time scale). Therefore, the accuracy of the stochastic model hinges on the accuracy of the single-phase results beside its aptitude to physically represent the turbulence fluctuations discarded by the filtering operation.

According to the predictions of the present LES and to the work of Breuer et al. (2006), relation (19) does not hold for the low Stokes numbers ($St < 0.2$). Indeed, the numerical results of the deposition efficiency versus Stokes number show an inflection point and approach zero for finite Stokes number unlike the exponential relation (19) that approaches zero only at $St = 0$.
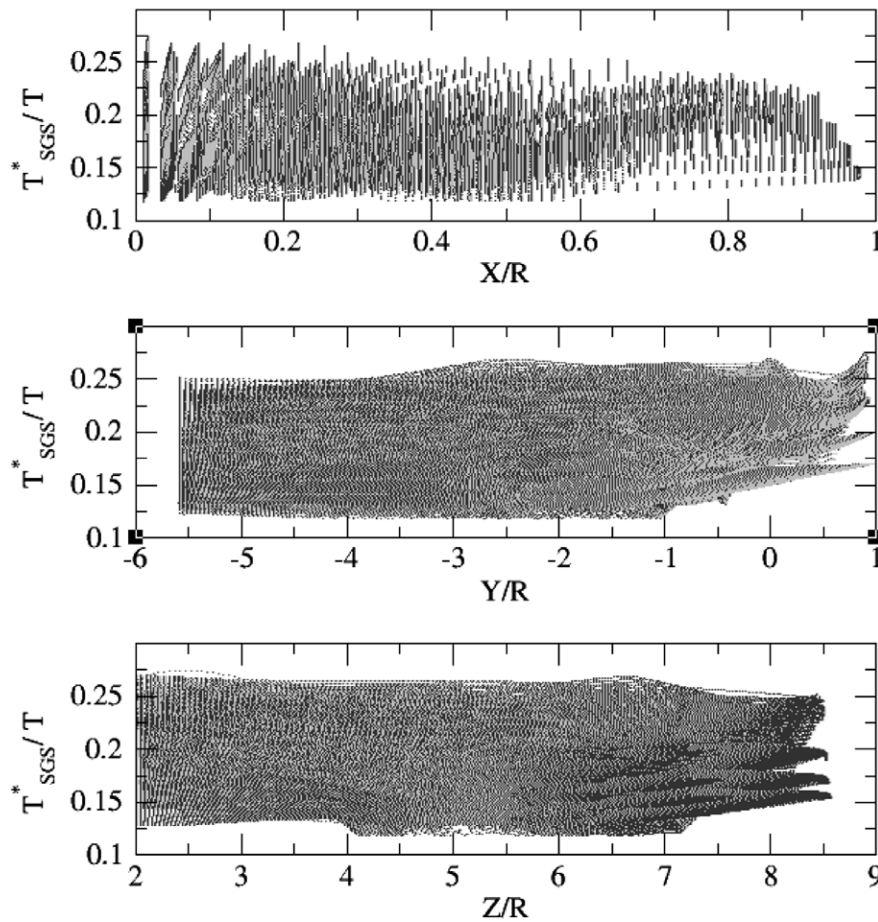
Fig. 13. Ratio of the sub-grid time scale $T^*_{SGS}$ to the integral time scale in different directions. $T = R/U_0$.

The effect of Stokes number on particle deposition behaviour is also investigated. Figs. 14 and 15 show the LES predictions of deposition patterns on the outer and inner bend respectively for nine different Stokes numbers. The small particles with low inertia are able to follow closely the continuous flow and are subject to all the turbulent fluctuations that are present in the flow with different time scales. They mostly exit the bend without depositing as it is shown on Fig. 14a, b and c. A small fraction of them deposits on the side walls or on the inner bend owing to the secondary motion as depicted in Fig. 15a, b and c.

Particles with intermediate Stokes number are more subject to inertia forces owing to their increased sizes. They respond to less and less turbulent fluctuations because of their growing Stokes numbers. Due to centrifugal forces, particles that are in the core region of the bend are entrained by the re-entrant jet and thus deposited on the outer bend while particles that are trapped in the counter-rotating Dean vortices exit the bend without depositing. For particles with Stokes number St = 0.27, a deposition on the outer bend is occurring only on the outermost radius as it is shown in Fig. 14d. For particles with Stokes numbers St = 0.46 and St = 0.75, the outer bend is covered completely with depositing particles as it is depicted in Fig. 14e and f. Owing to their increased inertia the last two classes of particles cease to follow the flow in the Dean

vortices and are driven toward the outer bend by the centrifugal forces. For this range of Stokes number, part of particles that exit the bend deposit on both sides of the straight pipe as it is shown in Fig. 15d, e and f.

Particles with large Stokes numbers (St > 1) do not follow the secondary flow in the bend. Thus, they almost all deposit at the outer bend because of the centrifugal force and only an insignificant number of these particles deposit on the inner bend or exit the bend. This fact is depicted in Fig. 15g, h and i.

It is noticeable in Fig. 15a to i that there is a long narrow band around the innermost radius where no deposition takes place. This fact is mentioned in Breuer et al. (2006) work but not reported in the experimental study of Pui et al. (1983). The reason for this phenomenon is the additional secondary flow structure consisting of a pair of counter-rotating small vortices at the inner bend radius that prevent particles from depositing along a stripe at a region around the innermost bend. As it was mentioned in Section 3.1, the fact that no particles deposit on the innermost radius of the bend is a proof of the existing of a pair of counter-rotating small vortices in that region of the bend. However, at 90° deflection, These structures do not appear in Fig. 9c because their sizes are underestimated by the present LES.

To investigate the effect of particle injection position on the deposition efficiency, the section of injection is divided
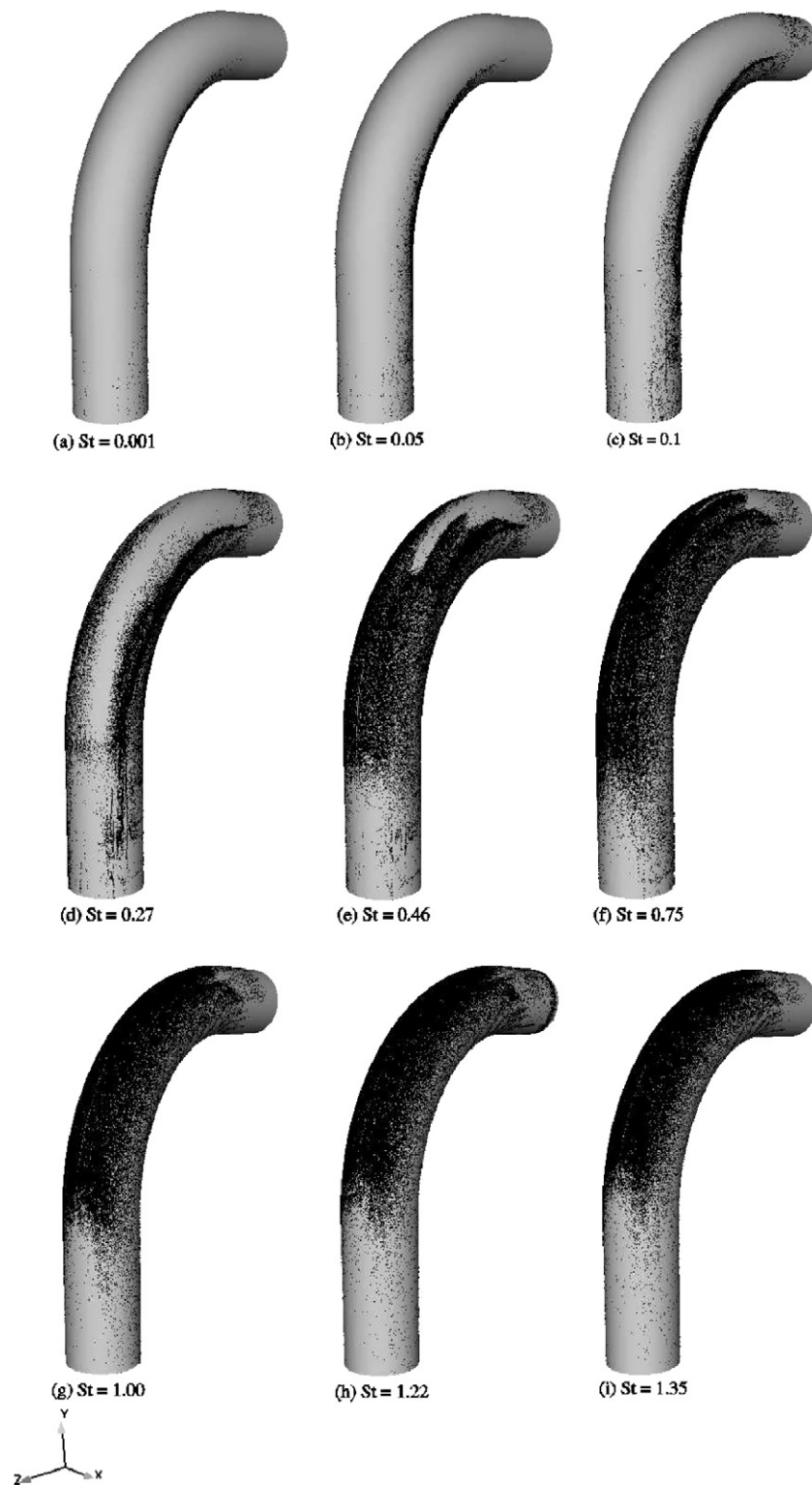
Fig. 14. LES predictions of particle deposition patterns on the outer bend at nine different Stokes numbers: (a) St = 0.001, (b) St = 0.05, (c) St = 0.1, (d) St = 0.27, (e) St = 0.46, (f) St = 0.75, (g) St = 1.00, (h) St = 1.22, (i) St = 1.35.

into 5 regions or bins $(N_b = 5)$ of equal surface area as it is shown in Fig. 16. Particles are injected randomly at the injection section and the number of deposited particles originating from the same region and deposited is computed and displayed in Fig. 17. For particle with Stokes number $St = 0.001$, no particle originating from zone 1

and 2 that represent the core region of the bend deposit on the bend walls. Around 60% of particles that came into contact with the bend walls are those that are injected near the wall from zone 5. The contribution of this zone to the number of depositing particles decreases with increasing Stokes number while more and more particles injected
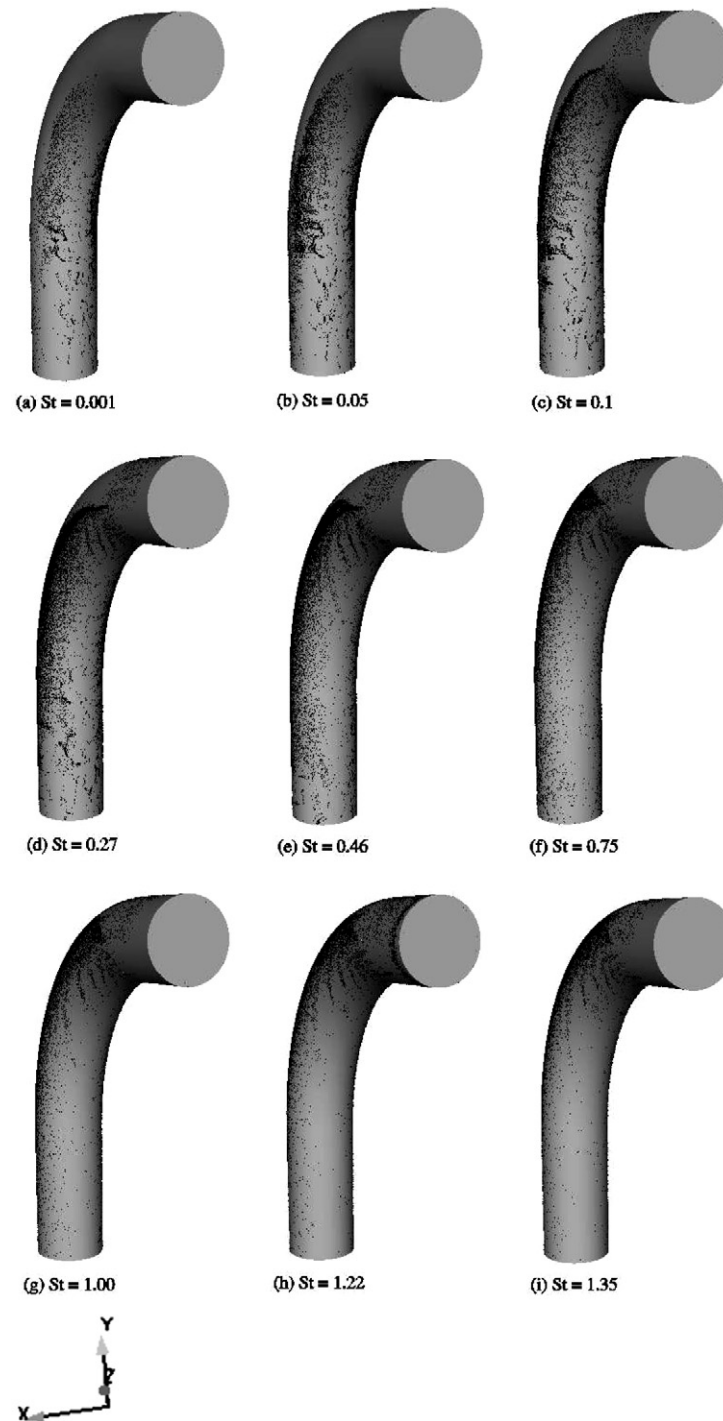
Fig. 15. LES predictions of particle deposition patterns on the inner bend at nine different Stokes numbers: (a) St = 0.001, (b) St = 0.05, (c) St = 0.1, (d) St = 0.27, (e) St = 0.46, (f) St = 0.75, (g) St = 1.00, (h) St = 1.22, (i) St = 1.35.

from zone 2 and 3 deposited. It is interesting to notice that particles with Stokes number up to St = 0.1 do not deposit if they are all injected from zone 1.

This remark could have an important practical use concerning the design of the Metered Dose Aerosol Inhalers (MDI) that are used to deliver medication through the mouth to the lungs for people with respiratory system diseases. It is well known that the smaller are the aerosols generated by these MDIs, the lower is their deposition rate in the

mouth and throat and by consequence the less are the drug's side effects. At the same time the smaller are the aerosols the more expensive is the device that generates them. The flow parameters that are studied herein and the geometry in which it takes place are similar to the flow in the mouth-throat geometry and consequently the main findings of this study can be used to design a cheap and efficient MDI. Indeed the results show that if particles are injected on the whole cross-section of the MDI's section of injection,
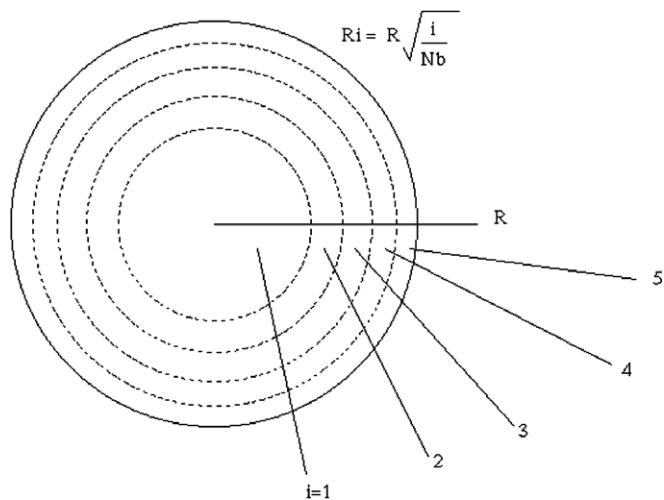
Fig. 16. Definition of equal area interval on the section of injection. R the radius of the section of injection. $N_b$ is the number of bins. i is the zone number.

particles with diameter as small as $d_p = 0.62\mu m\ (St = 0.001)$ should be generated in order to have an insignificant deposition in the mouth-throat region. However, if the injection is confined to the core region of the MDI's section of injection $(r < \sqrt{0.2}R)$, insignificant deposition occurs for particle diameter as large as $d_p = 6.8\mu m(St = 0.1)$. It is important to mention that although the $0.62\mu m$ particles are suggested for usage in MDIs, they are not commonly used because they can be easily exhaled (before deposition in the lungs) after inhalation. Also, MDI aerosol deposition is also a function of the inhalation flow rate or flow Reynolds number.

### 3.3. Computational requirements

The total computational times associated with the use of the present grid resolution and a grid resolution similar to the one of Breuer et al. (2006) are shown in Table 5. The

overhead associated with the stochastic model evaluation is about 3% of the two-phase LES CPU time and approximatively 17% of the discrete phase CPU time. When a grid resolution similar to the one adopted by Breuer et al. (2006) was considered, the single-phase LES CPU time increased of almost 43% as compared to the CPU cost of the present LES. Also the overhead associated with particle tracking increased because the trajectory engine needs to perform more tests while going through a denser grid ($\approx 10\%$ increase). Thus the use of the grid resolution of Breuer et al. (2006) to perform a two-phase LES (obviously a stochastic model is not needed) resulted in an increase of the CPU time of about 34%. This justifies the use of a coarser grid coupled with a stochastic model for the present two-phase LES.

## 4. Concluding remarks

A well-resolved LES was performed to study aerosol deposition in a turbulent 90° bend flow with tubular

Table 5
Computer requirements for the single- and two-phase LES calculations using the present grid resolution and the one adopted by Breuer et al. (2006)

|  | Resolution (million of cells) | $N_p$ (million of particles) | Normalized CPU time |
|---|---|---|---|
| Single-phase LES | 1.3 |  | 1 |
| Two-phase LES without stochastic modelling | 1.3 | 0.25 | 1.174 |
| Two-phase LES with stochastic modelling | 1.3 | 0.25 | 1.209 |
| Single-phase LES | 2.28 |  | 1.427 |
| Two-phase LES without stochastic modelling | 2.28 | 0.25 | 1.623 |

One unit corresponds to 253 seconds of CPU time per time step on one processor of an Optiplex GX260.
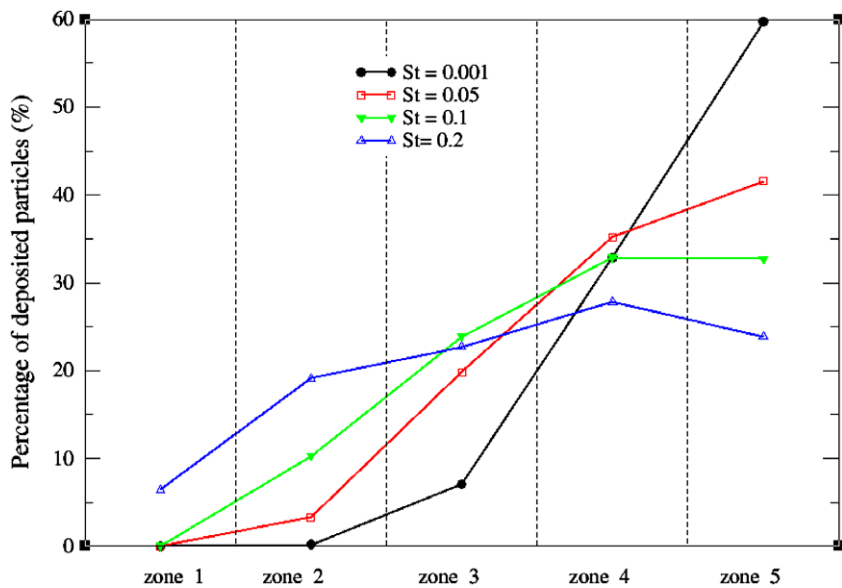


Fig. 17. Percentage of deposited particles per zone of injection. St is the Stokes number. Different zones of injection are defined in Fig. 16.

cross-section. Numerical predictions were compared to the experimental observations of Pui et al. (1983) and the fully-resolved LES of Breuer et al. (2006).

Due to the complexity of the turbulent flow in curved pipe characterized by curved streamlines and zones of recirculation and the lack of comparison studies of the same flow parameters, a good deal of care has been taken to ensure that the simulation of the carrier phase is reasonably accurate. Efforts was made to adapt the mesh to the dynamical features of the flow and boundary conditions were set such the inlet and outlet conditions would not influence the turbulent flow in the bend. The numerical predictions of the secondary flow and streamlines in the symmetry plane and in cross-sections at different angle of deflection showed a good qualitative agreement with the fully-resolved LES of Breuer et al. (2006) though some discrepancies were noticed in some regions of the bend. This is mainly due to differences of grid resolution and distribution of cells, in particular in the cross-sections, between the two simulations. *A-posteriori* estimation of the filtered-out kinetic energy demonstrated that the present LES is adequate according to the LES index of quality developed by Celik et al. (2003) and Pope (2004).

For the dispersed phase, a stochastic model that accounts for inertial particle transport by SGS motion was used. It was anticipated that such modelling should be crucial owing to the very small-Stokes-number particles tracked. An estimation of the time scale of the SGS fluctuations that are discarded by the filtering operation in LES showed clearly those particles with Stokes number smaller than 0.29 do sense the SGS turbulent fluctuations

Numerical results concerning the deposition efficiency of inertial particles with Stokes number that ranges between 0.005 and 1.5 demonstrated the ability of the stochastic modelling to reproduce with good accuracy the SGS effects on small-Stokes-number particles. As it was expected the use of the filtered velocity field only (no stochastic modelling ) to track particles with Stokes number smaller than 0.3 has proven inaccurate.

The influence of the injection position of the small particles on their deposition efficiency was investigated. It was shown that, if injected in the core region of the bend ($r < \sqrt{0.2}R$), particles with diameter as large as $6.8\mu m (St = 0.1)$ can exit the bend without depositing.

The present study shows that the deposition efficiency of small inertial particles can be predicted with a good accuracy in the framework of LES using a coarse numerical description. To remove uncertainties tied to the effect of the SGS motion on inertial particle transport, SGS models for particles should be taken into account. The Langevin-type stochastic diffusion process used in this work has proven very adequate in this regard.

The use of a coarser numerical description coupled with a stochastic modelling of the SGS motion provided substantial savings compared to a fully-resolved two-phase LES, as the CPU time necessary for the evaluation of the SDE system contributes to only a small fraction of the CPU time of the discrete phase simulation.

The effect of SGS modelling becomes increasingly important with higher Reynolds number non-equilibrium turbulent flows where resolving all the relevant scales becomes computationally prohibitive. In future the performance of the present model needs to be further assessed for such flows.

### Acknowledgement

### Appendix. Analytical Solution of the SDE System

The analytical solutions of the SDE system (4.15) for particle position $x_p$, velocity $u_p$ and seen fluid velocity $u_s$ are given below:

$$u_{s,i}(t) = u_{s,i}(0)\exp(-\Delta t/T^*_{SGS}) + [\bar{u}_i + T^*_{SGS}\Pi_i]\{1 - \exp(-\Delta t/T^*_{SGS})\} + \gamma_i(t),$$

$$u_{p,i}(t) = u_{p,i}(0)\exp(-\Delta t/\tau_p) + u_{s,i}(0)\left(\frac{1}{1 - \tau_p/T^*_{SGS}}\right)\{\exp(-\Delta t/T^*_{SGS}) - \exp(-\Delta t/\tau_p)\}$$

$$+ \tau_p g_i(1 - \exp(-\Delta t/\tau_p)) + \Gamma_i(t),$$

$$x_{p,i}(t) = x_{p,i}(0) + u_{p,i}(0).\Delta t.[1 - \exp(-\Delta t/\tau_p)]$$

$$+ u_{s,i}(0)\left(\frac{1}{1 - \tau_p/T^*_{SGS}}\right) \times \{T^*_{SGS}[1 - \exp(-\Delta t/T^*_{SGS})] + \tau_p[1 - \exp(-\Delta t/\tau_p)]\}$$

$$+ [\bar{u}_i + T^*_{SGS}\Pi_i]\{\Delta t + \tau_p(\exp(-\Delta t/\tau_p) - 1)$$

$$- \left(\frac{1}{1 - \tau_p/T^*_{SGS}}\right) \times \{T^*_{SGS}[1 - \exp(-\Delta t/T^*_{SGS})] + \tau_p[1 - \exp(-\Delta t/\tau_p)]\}$$

$$+ \tau_p g_i(\Delta t - \tau_p(\exp(-\Delta t/\tau_p))) + \Omega_i(t).$$

Where:

$$\Pi(i) = -\frac{1}{\rho_f}\frac{\partial \bar{p}}{\partial x_i} + \frac{1}{Re}\frac{\partial^2 \bar{u}_i}{\partial x_j \partial x_j},$$

$$\gamma_i(t) = \sqrt{C_0^* <\epsilon_r>}\exp(-\Delta t/T_{SGS}^*)\int_0^t \exp(-t'/T_{SGS}^*)\mathrm{d}W_i,$$

$$\Gamma_i(t) = \frac{1}{\tau_p}\exp(-\Delta t/\tau_p)\int_0^t \exp(-t'/\tau_p)\gamma_i(t')\mathrm{d}t',$$

$$\Omega_i(t) = \int_0^t \Gamma_i(t')\mathrm{d}t'.$$

# References

Archambeau, F., Mehitoua, N., Sakiz, M., 2004. *Code_Saturne:* A finite-volume code for the computation of turbulent incompressible flows - industrial applications. Int. J. Finite Vol. 1, 1–62.

Armenio, V., Piomelli, U., Fiorotto, V., 1999. Effect of the sub-grid scales on particle motion. Phys. Fluids 11, 3030–3042.

Berger, S.A., Talbot, L., Yao, L.S., 1983. Flow in curved pipes. Ann. Rev. Fluid Mech. 15, 461–512.

Berrouk, A.S., Laurence, D., Riley, J.J., Stock, D.E., 2007. Stochastic modelling of inertial particle dispersion by subgrid motion for LES of high Reynolds number pipe flow. J. Turbulence 8, 50.

Boersma, B.J., Nieuwstadt, F.T.M., 1996. Large-eddy simulation of turbulent flow in a curved pipe. J. Fluids Eng. 118, 248–254.

Breuer, M., Baytekin, H.T., Matida, E.A., 2006. Prediction of aerosol deposition in 90° bends using LES and an efficient Lagrangian tracking method. J. Aerosol Sci. 37, 1407–1428.

Celik, I.B., Cehreli, Z.N., Yavuz, I., 2003. Index of quality for large-eddy simulations. In: Proceedings of ASME FEDSM2003-45448, 4th ASME JSME Joint Fluids Engineering Conference, Honolulu, Hawaii.

Csanady, G.T., 1963. Turbulent diffusion of heavy particles in the atmosphere. J. Atmos. Sci. 20, 201–208.

Eggels, J.G.M., Nieuwstadt, F.T.M., 1993. Large-eddy simulations of turbulent flow in an axially rotating pipe. In: Proceedings of the 9th Symposium on Turbulent Shear Flows. Poster Paper 310. pp 1–4.

Finlay, W.H., 2001. The Mechanism of Inhaled Pharmaceutical Aerosols: An Introduction. Academic Press, London.

Gicquel, L.Y.M., Givi, P., Jaberi, F.A., Pope, S.B., 2002. Velocity filtered density function for large eddy simulation of turbulent flows. Phys. Fluids 14, 1196.

Heinz, S., 2003. Statistical Mechanics of Turbulent Flows. Springer-Verlag, Berlin.

Kloeden, P.E., Platen, E., 1999. Numerical Solution of SDE Through Computer Experiment. Springer-Verlag, New York.

Lakehal, D., 2002. On the modelling of multiphase turbulent flows for environmental and hydrodynamic applications. Int. J. Multiphase Flows 28, 823–863.

Langevin, P., 1908. Comptes Rendus. Acad. Sci. 146, 530–533.

Laurence, D., 2006. Large eddy simulation with Unstructured Finite Volumes. Direct and Large Eddy Simulations VI. ERCOFTAC Series 10, 27–38.

Maclnnes, J.M., Bracco, F.V.H., 1992. Stochastic particle dispersion modelling and the tracer-particle limit. Phys. Fluids 12, 2809–2824.

Maxey, M.R., Riley, J.J., 1983. Equation of motion for a small rigid sphere in a nonuniform flow. Phys. Fluids 26, 883–889.

Minier, J-P., Peirano, E., 2001. The PDF approach to turbulent polydispersed two-phase flows. Phys. Rep. 352, 1–214.

Minier, J-P., Peirano, E., Chibbaro, S., 2003. Weak first and second order numerical schemes for stochastic differential equations appearing in Lagrangian two-phase flow modelling. Monte Carlo Methods Appl. 9, 93–133.

Minier, J-P., Peirano, E., Chibbaro, S., 2004. PDF model based on Langevin equation for polydispersed two-phase flows applied to a bluff-body gas-solid flow. Phys. Fluids 18, 302–314.

Pope, S.B., 2004. Ten questions concerning the large-eddy simulation of turbulent flows. New J. Phys. 6, 35.

Pozorski, J., Minier, J-P., 1998. On the Lagrangian turbulent dispersion models based on the Langevin equation. Int. J. Multiphase Flow. 24, 913–945.

Pui, D.Y.H., Romay-Novas, F., Liu, B.Y.H., 1987. Experimental study of particle deposition in bend of circular cross-section. Aerosol Sci. Technol. 7, 301–315.

Sato, Y., Yamamoto, K., 1987. Lagrangian measurement of fluid-particle motion in an isotropic turbulent field. J. Fluid Mech. 175, 183.

Shotorban, B., Mashayek, F., 2006. A stochastic model for particle motion in large-eddy simulation. J. Turbulence 7, 18.

Smagorinsky, J., 1963. General circulation experiments with the primitive equations. Mon. Weather Rev., 91–99.

Wang, L.P., Stock, D.E., 1993. Dispersion of heavy particles by turbulent motion. J. Atmos Sci. 50, 1897–1913.